Antiferromagnetic correlations in Fe–Cu granular alloys: The role of the surface structure

Xavier Batlle[a)]
Dept. Física Fonamental, Facultat de Física, Universitat de Barcelona, Diagonal 647, Barcelona 08028, Catalonia, Spain and National Center for Electron Microscopy, Lawrence Berkeley National Laboratory, University of California, 1 Cyclotron Road, Berkeley, California 94720

Chuck J. Echer, E. Chris Nelson, and Kannan M. Krishnan
National Center for Electron Microscopy, Lawrence Berkeley National Laboratory, University of California, 1 Cyclotron Road, Berkeley, California 94720

Bart Jan Hattink
Dept. Física Fonamental, Facultat de Física, Universitat de Barcelona, Diagonal 647, Barcelona 08028, Catalonia, Spain

(Received 26 July 1999; accepted for publication 14 December 1999)

Fe precipitates in a Cu_{fcc} matrix, prepared using the Bridgeman method and with an average composition of $Cu_{97}Fe_3$, displayed the coexistence of ferromagnetism (FM), spin glass-like (SGL) behavior and antiferromagnetic (AFM) correlations. The two former contributions may be attributed, respectively, to the segregation of FM, α-Fe_{bcc} precipitates and to the few Fe spins distributed in the matrix. The annealing procedures increased the FM contribution and, as particle growth and phase segregation took place, the SGL behavior progressively disappeared. Results from high resolution transmission electron microscopy (HRTEM), x-ray photoelectron spectroscopy (XPS), and electron energy-loss spectroscopy (EELS) suggest that the AFM correlations are due to the α-Fe particles that show a surface layer of a few nanometers in thickness, of either FeO and/or γ-Fe_{fcc}. XPS and EELS measurements confirm the presence of FeO; however, the latter is only tentatively suggested by the HRTEM analysis of the particle/matrix interfaces. © *2000 American Institute of Physics.* [S0021-8979(00)08106-8]

I. INTRODUCTION

Heterogeneous granular alloys consisting of a distribution of small ferromagnetic (FM) precipitates embedded in a nonmagnetic metallic (NM) matrix have been extensively studied over the last few years because they exhibit giant magnetoresistance (GMR).[1,2] Typical granular alloys are Co–Ag, Co–Cu, Fe–Cu, CoFe–Ag, NiFe–Ag, and CoFe–Cu; and depending on the relative FM–NM miscibility, as deposited samples (prepared, for instance, by sputtering) are usually annealed at temperatures between 450 and 700 °C in order to promote the segregation and growth of the FM particles. The maximum GMR effect observed at low temperatures is ~30%–40% and this is obtained at ~20–25 at. % FM concentration. Spin glass-like (SGL) behavior has also been reported at low FM concentrations,[1] and is related to the degree of FM–NM alloying. In general, FM–NM alloys are well known for showing this glassy behavior even at FM concentrations as low as about 0.01 at. %.[3] Heterogeneous alloys are also of importance in understanding the basic properties of a distribution of small magnetic particles. These alloys allow us to study the two main features that determine the magnetic properties of fine particle systems, i.e., the crystallographic and chemical structure at particle surfaces and the magnetic correlations. Moreover, GMR in granular alloys is essentially related to the spin-dependent scattering of conduction electrons at the particle–matrix interfaces and this effect is monitored by the demagnetization mechanism occurring at the particle surface.[4]

In this article we discuss the structural and magnetic properties of Fe precipitates grown in a Cu matrix by annealing a precursor alloy of composition $Cu_{97}Fe_3$ under various conditions. A low Fe content was chosen to obtain a distribution of isolated magnetic particles, so as to study the structure of the particle surface and its contribution to the magnetic properties. Moreover, this is an ideal system by which to evaluate the crystallographic relationships between the magnetic precipitates and the matrix, and the way in which these orientation relationships affect the magnetotransport (GMR) properties of these alloys. This article is thus aimed at correlating the crystal structure with the magnetic properties and at identifying the key structural factors responsible for the coexistence of ferromagnetism, antiferromagnetic (AFM) correlations, and SGL behavior in these low ferromagnet content Fe–Cu heterogeneous alloys. We note that although coherent γ-Fe precipitates in a Cu matrix are paramagnetic at room temperature and antiferromagnetic below ~70 K, it is not yet clear how interfacial strains and interdiffusion affect the AFM correlations when thin γ-Fe films are grown on Cu[5] and even how room temperature ferromagnetic γ-Fe films may be obtained.[6]

a)Author to whom correspondence should be addressed: Permanent address: Dept. Física Fonamental, Facultat Física, Universitat Barcelona, Diagonal 647, Barcelona 08028, Catalonia (Spain); Electronic mail: xavier@ffn.ub.es

II. EXPERIMENT

Cu–3 at. % Fe alloys were grown using the Bridgeman method and individual pieces were annealed under various conditions: samples A (650 °C, 18 min), B (650 °C, 4 h), C (650 °C, 24 h), and D (700 °C, 70 h). X-ray diffraction (XRD) patterns in the $\theta/2\theta$ geometry and transmission electron microscopy (TEM) in bright (BF) and dark field (DF) modes were used to determine the average crystal structure and particle size of the matrix and precipitates. The local and average compositions were evaluated by x-ray energy-dispersive spectrometry (XEDS) using a 20 nm electron probe in a standard JEOL 200 CX microscope equipped with a scanning TEM (STEM) unit. X-ray maps of Cu, Fe, and O were also obtained from XEDS. Selected area electron diffraction (SAED) and microdiffraction experiments with a 20 nm electron probe were recorded to ascertain the local structure and orientation relationships. High resolution TEM was performed using a Philips CM 200 FEG microscope. This microscope also incorporated an electron probe of ~1–2 nm and was used to determine the local structure and orientation relationships at the nanometer scale. The particle/matrix interfaces were also studied. Energy filtered images were obtained by electron energy-loss spectrometry (EELS) in a Philips CM 300 FEG microscope in order to map the Cu, Fe, and O distributions. X-ray photoelectron spectroscopy (XPS) using Al and Mg Kα sources made it possible to evaluate the content of both metallic Fe and Fe–O in the samples. Hysteresis loops, with applied fields up to 12 kOe, were measured at room temperature using a vibrating sample magnetometer and ac susceptibility (ac magnetic field of 1 Oe). The latter was measured as a function of temperature (4.2–275 K), frequency (11–1111 Hz), and dc applied magnetic field.

III. RESULTS AND DISCUSSION

XRD and TEM showed that α-Fe_{bcc} particles precipitate in the Cu_{fcc} matrix[7] and grow as the annealing time increases. No other phases, such as γ-Fe_{fcc}, Cu–O, or Fe–O, were detected. Average sizes were obtained from the peak broadening of the XRD spectra of the samples, in comparison to a Cu_{fcc} standard, which was used to calibrate both the position and the instrumental width of the diffraction peaks. Crystallographic Cu domains ranged from a few tenths of a micron to a few microns; due to the small Fe concentration, their peak positions were not affected, within the experimental error, by the annealing procedure. The average size of the α-Fe precipitates, obtained from the $Fe_{(011)}$ peak, was ~27, ~39, and ~58 nm for samples B, C, and D, respectively (Fig. 1). These values are in agreement with the particle sizes observed by DF TEM images, which ranged from 6 to 15 nm in sample A, 15 to 30 nm in sample B, 30 to 60 nm in sample C, and 40 to 70 nm in sample D. The integrated intensity of the $Fe_{(011)}$ peak increased with the annealing time (this effect was particularly noticeable when going from sample B to C), suggesting that Fe segregation also occurred. The XRD spectra may be fitted within the range $2\theta = 42°–46°$, if we take into account the $Cu_{(111)}$ and $Fe_{(011)}$ peaks. Unfortunately, for this low Fe concentration, XRD cannot detect γ-Fe precipitates, especially if they are coherent with the Cu matrix.

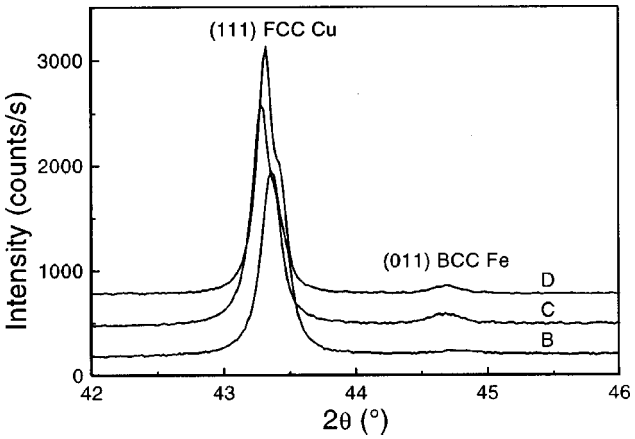

FIG. 1. Detail of the XRD spectra for samples B, C, and D.

From the integrated intensities of these two peaks, the atomic α-Fe concentration was found to be about 4% for sample D. The isolated α-Fe precipitates are shown in the DF TEM micrographs [Fig. 2(c)].

The local and average composition of the samples was determined by x-ray energy-dispersive spectrometry (XEDS) using a 20 nm electron probe. Both x-ray line profiles and maps (not shown) suggest that Fe-rich regions corresponded to the imaged particles, while the average composition obtained by scanning the electron probe in a 1×1 μm was ~2.5 at.% Fe for sample B and ~5.5 at.% Fe for sample C. Although this difference can be attributed to the experimental error in the measurement, it is in agreement with the increase in Fe segregation with the annealing time detected from XRD, and with both the hysteresis loops (Fig. 8) and temperature dependence of the ac susceptibility (Figs. 6 and 7). The local composition was obtained using an ultrathin window detector; when the beam was focused on a thick area

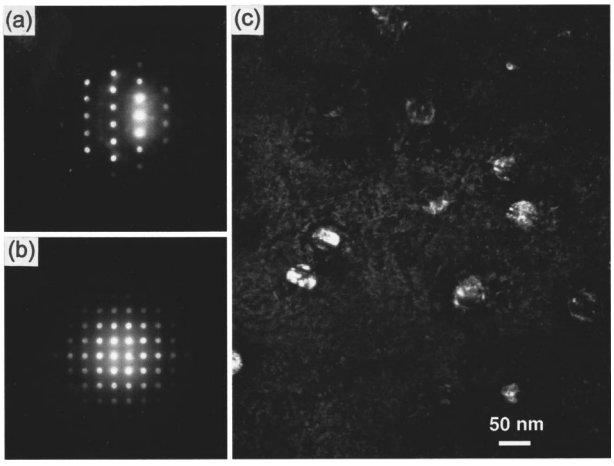

FIG. 2. Microdiffraction patterns for sample C, using a 20 nm electron probe: (a) [013] zone axis for the Cu_{fcc} matrix and (b) [001] zone axis for an Fe_{bcc} precipitate. The camera constant was calibrated from the Cu diffraction pattern and used to index that of the Fe, always resulting in a bcc structure in the case of the latter. (a) and (b) do not represent the orientation relationships between the precipitates and the matrix, since the diffraction patterns of the matrix and precipitate were obtained in different areas and orientations (tilts) of the sample. (c) DF TEM micrograph for sample C, showing isolated α-Fe particles.

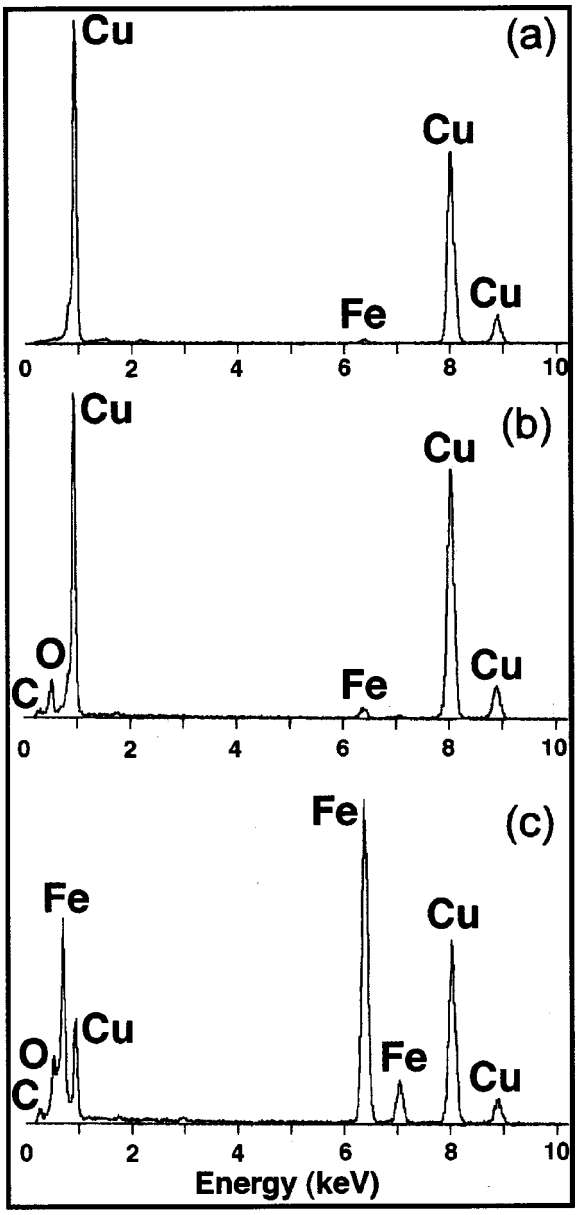

FIG. 3. XEDS spectra for sample D, using a 20 nm electron probe and an ultrathin window detector: (a) thick area of the Cu matrix (360 counts/s), (b) thin area (near the hole in the sample) of the Cu matrix (30 counts/s), (c) Fe precipitate ~40 nm in diameter (30 counts/s) in an area close to (b). The total number of counts was 100,000 in all cases. Some surface C contamination is present in (b) and (c). (c) confirms that the precipitates are Fe rich. Oxygen is mainly located at the sample surface [O peak is present in (b) and (c), but not in (a)]. However, some extra oxygen might be located in the Fe-rich precipitates. All spectra were performed after cleaning the sample surface by ion milling in LN_2.

of the matrix, the expected Cu-dominant spectrum was obtained and no O contribution was detected [Fig. 3(a)]. In contrast, when the beam was focused on a thin area of the matrix, the expected surface O contamination (passivation layer) was clearly visible [Fig. 3(b)]. Finally, when the beam was focused on top of an imaged precipitate [on an area very near to the previous spectrum and of very similar thickness since the counting rate was roughly the same—Fig. 3(c)], even though the spectrum was dominated by the contribution from Fe, the O contribution was slightly higher (~4% for sample D) than before, suggesting that some extra O might

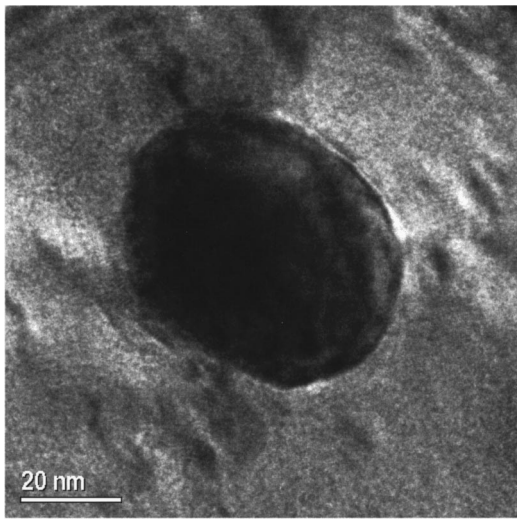

FIG. 4. HRTEM image for sample C, showing the ellipsoidal distortion of some of the α-Fe particles.

be located in the Fe-rich precipitates, leading to both metallic Fe and an Fe–O-type compound in the precipitates. However, the latter result should be taken as tentative since it might be related to a higher surface roughness around the Fe precipitates. We note that, based on the x-ray maps for Fe and O in very thin areas of the samples, oxygen was uniformly distributed throughout the sample and it did not correlate with the Fe-rich precipitates.

Microdiffraction patterns were recorded with a 20 nm electron probe to ascertain the crystal structure of the Fe precipitates. The Cu matrix was oriented along a given zone axis, from which the camera constant **c** was determined by applying the expression $r(h,k,l)\cdot d(h,k,l)=\mathbf{c}$; where $r(h,k,l)$ is the experimental distance from the transmitted beam to the diffraction spot and $d(h,k,l)$ the ideal fcc $Cu_{(h,k,l)}$ interplanar spacing [Fig. 2(a)]. Applying this value of **c**, indexing of the microdiffraction patterns of the Fe particles always led to a bcc structure [Fig. 2(b)]. The bcc structure of the Fe precipitates and the particle/matrix orientation relationships were checked at the nanometer scale using a 2.4 nm electron probe. First, an Fe precipitate was imaged by HRTEM (Fig. 4). Then, the sample was tilted until the microdiffraction pattern indicated that the [111] zone axis for the Cu_{fcc} matrix surrounding the Fe precipitate had been reached [Fig. 5(a)]. Finally, whenever the microdiffraction pattern was taken at the center of the Fe precipitate, the [110] zone axis for Fe_{bcc} was obtained [Fig. 5(b)], yielding the Kurdjumov–Sachs orientation relationships for fcc and bcc grains[8]—$[111]_{fcc\,Cu}||[110]_{bcc\,Fe}$ and $(1-10)_{fcc\,Cu}||(1-11)_{bcc\,Fe}$. As usual, the camera constant was calibrated from the Cu diffraction pattern and used to index the Fe pattern. However, a mismatch between the zone axes of the matrix and precipitate, which increased with the annealing temperature, was detected. The mismatch angles were ~0°, 1.5°, 3°, and 5.5°, for samples A, B, C, and D, respectively. This may be related to the particle distortion as a function of growth from quasispherical to ellipsoidal-like and observed in HRTEM images (Fig. 4). Small quasispherical bcc particles may be accommodated in a fcc matrix and although

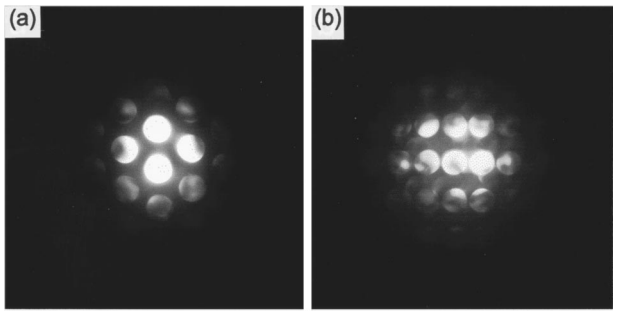

FIG. 5. Microdiffraction patterns for sample D, using a 2.4 nm electron probe: (b) [110] zone axis at the center of an Fe_{bcc} precipitate ~50 nm in diameter and (a) [111] zone axis for the Cu_{fcc} matrix all around the Fe precipitate. (a) and (b) show the Kurdjumov–Sachs orientation relationships for fcc and bcc grains (Ref. 8). Patterns (a) and (b) are related through a tilting angle of about 5.5° and this slight mismatch is associated with the anisotropic growth of the particles.

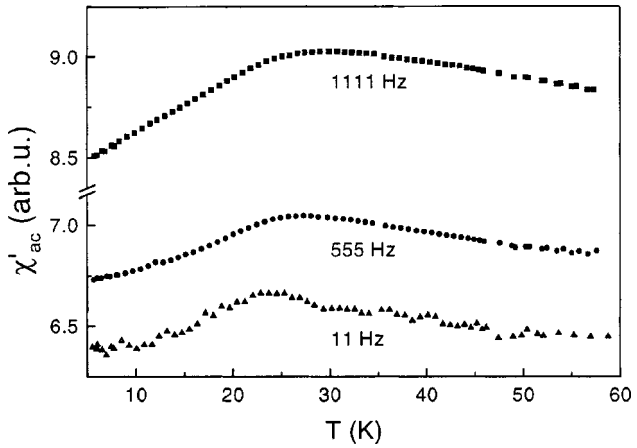

FIG. 7. Detail of the in-phase component of the ac susceptibility χ'_{ac} at low temperature for sample B at different frequencies.

this leads to a large local surface strain (the cell parameters have to match at the particle/matrix interface), the overall surface energy is small. Larger particles cannot accommodate the local strain at the surface, so they grow ellipsoidal-like, at the expense of an increase in the surface energy. This kind of deformation is common in Fe-Cu alloys.[8]

The ac susceptibility measurements with an ac field of 1 Oe and at six frequencies, ranging from 11 to 1.1×10^4 Hz, were carried out between 4.2 and 275 K. Both samples A and B clearly showed a characteristic SGL peak in the in-phase component, χ'_{ac}, at low temperature (Fig. 6). No relevant differences were observed in these two samples. The freezing temperature depends on the measured frequency and shifted from ~23 K at 11 Hz to ~30 K at 1.1×10^3 Hz, for sample B (Fig. 7). This low-temperature peak is also dependent on the application of a dc field (parallel to the ac field) and it shifted from ~27 ($H_{dc}=0$) to ~35 K when $H_{dc}=500$ Oe for sample B, with a measuring frequency of 111 Hz, as observed in other small particle systems.[9] Samples C and D did not display this peak; however, χ'_{ac} increased below about 20 K, suggesting that the SGL behavior, if present, would appear only below 4.2 K. This is in agreement with increasing Fe segregation with annealing time, since the concentration of isolated Fe spins diluted in the matrix, which are responsible for this freezing behavior, is drastically reduced. A residual Fe dilution of ~0.3 at. % in sample D might lead to a freezing temperature of about 2 K,[3] which is in agreement with the expected solubility of Fe in Cu (0.35 at. % Fe in Cu at 780 °C), obtained from the phase diagram.[7] Finally, a clear increase in χ'_{ac} was observed above 80 K for all samples, and this increase was smoothed by the application of a dc field. These findings suggest the presence of short-range AFM correlations which are broken by a dc field, in agreement with the magnetization curves (Fig. 8, see below), although this AFM contribution might be partially hidden by the increase in the background signal coming from the FM phase (increasing with the dc applied field). This FM contribution should give a quasiconstant χ'_{ac} since the initial susceptibility of a distribution of blocked FM particles does not depend on temperature at temperatures well below the mean blocking temperature (flat zero-field cooling at low temperatures). These high-temperature AFM correlations were also observed in a $Cu_{5\,nm}/Fe_{0.5\,nm}$ multilayers (300 bi-

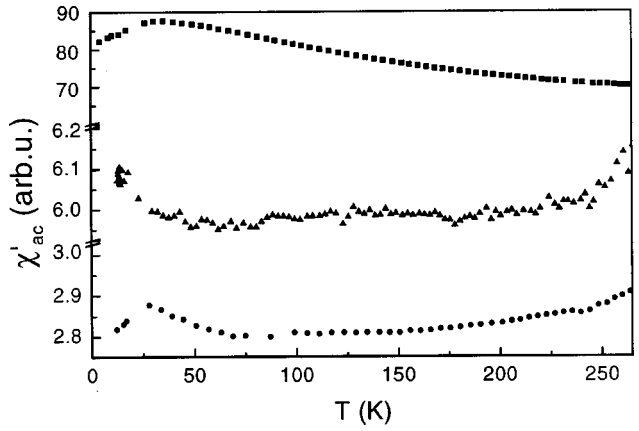

FIG. 6. In-phase component of the ac susceptibility χ'_{ac}: (●) sample B measured at 111 Hz, (■) sample B measured at 111 Hz and with a dc applied field of 500 Oe (parallel to the ac field), and (▲) sample D measured at 111 Hz.

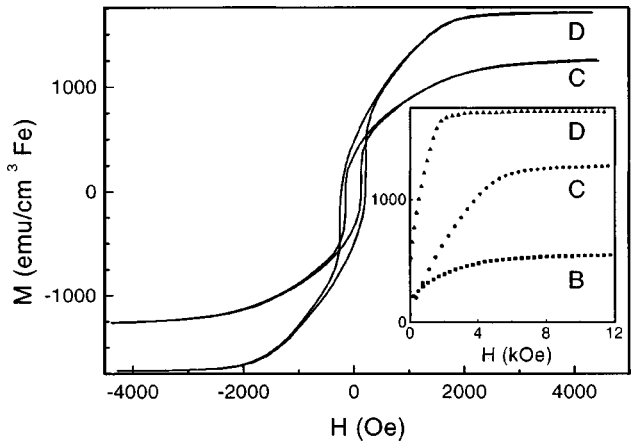

FIG. 8. Detail of the hysteresis loop at room temperature for samples C and D. Inset. Decreasing branch of the hysteresis loop at room temperature for samples B, C, and D. All curves have been normalized to the volume fraction of α-Fe precipitates obtained for sample D.

layers), which suggests that those samples may in fact comprise Fe clusters precipitated in a Cu matrix.[5] The low field susceptibility showed a blocking behavior at low temperature (very small α-Fe precipitates), while γ-Fe was only detectable by conversion electron Mössbauer spectroscopy.

Hysteresis loops measured at room temperature are plotted in Fig. 8. If we assume that the mean blocking temperature $\langle T_B \rangle$ and the energy of anisotropy $K \cdot \langle V \rangle$, ($K$ being the anisotropy constant, where $K_{\alpha-\text{Fe bulk}} = 4.72 \times 10^5$ erg/cm^3 at room temperature and $\langle V \rangle$ the mean particle volume), are related through the expression $K \cdot \langle V \rangle = 25 k_B \cdot \langle T_B \rangle$,[10] then most of the α-Fe particles must be blocked well above room temperature for samples B, C, and D, and we should expect a pure FM hysteresis loop. However, it could be argued that the increase in χ'_{ac} observed above 80 K (Fig. 6) might be related to the blocking of the smallest particles in samples A and B, rather than to short range AFM correlations. This is not possible for samples C and D, given the particle size distributions observed by TEM. Coercive fields range from 165 to 230 Oe for samples A and D, respectively, which are reasonable values for α-Fe (Fig. 8). All the samples saturated at large fields (Fig. 8, inset) and as the annealing time increased, saturation magnetization increased due to the decrease in both the amount of Fe spins alloyed to the Cu matrix and the relative unimportance of disordered spins at the particle surface (decrease in the surface-to-volume ratio), as well as the particle growth (negligible contribution from small particles that are not blocked at room temperature). However, for sample D (largest Fe segregation, largest α-Fe content), we obtained an experimental saturation magnetization $M_s^{\text{exp}} = 511$ emu/cm^3(Fe), which is much smaller than the expected bulk value $M_s = 1717$ emu/cm^3. This means that only about 30% (in volume) of the Fe content contributed to the saturation magnetization.

Let us assume that we have an inner FM particle core (α-Fe) and an outer shell not contributing to the magnetization. Then, M_s and M_s^{exp} are related through the expression $M_s^{\text{exp}} = M_s \cdot (1 - d \cdot \langle S \rangle / \langle V \rangle)$, where d is the thickness of the surface layer noncontributing to the saturation magnetization and $\langle S \rangle$ the mean particle surface. This expression yields $d = 6$ nm for sample D. The surface layer might have either a different crystal structure from that of the particle core, e.g., γ-Fe (Néel temperature $\sim$70 K[3,6]), or a different chemical composition, e.g., FeO (Néel temperature $\sim$186 K and extrapolated Curie–Weiss temperature $\sim$570 K), and these two possibilities might lead to the short-range AFM correlations observed at room temperature. The former might be caused by the matrix-particle interdiffusion and surface strains, yielding a progressive transformation from a bcc to a fcc structure of the Fe atoms at the particle surface. As $d \sim 10\%$ of the mean particle size, XRD cannot solve the problem of detecting the γ-Fe contribution, particularly if these small precipitates are coherent with the Cu matrix. Hence, all hysteresis loops (Fig. 8 and inset) have been normalized to the volume fraction of α-Fe precipitates obtained for sample D. It is also worth noting that the hysteresis loops (Fig. 8) suggest a superimposition of an inner FM-like loop (showing hysteresis) and an outer loop, which shows no hysteresis and a marked decrease in the slope (quasilinear M *versus* H curve). The latter contribution might be attributed to the short-range AFM correlations observed in the ac susceptibility, which are broken by the applied field as we approach saturation. This might be the reason why the knee of the loops (saturation field of about 1500 Oe) is reached at fields much higher than the field at which hysteresis disappears (which is of the order of the anisotropy field of α-Fe, i.e., a few hundred Oe) and the remanence-to-saturation ratio is much smaller than the value expected for a cubic system. In addition, some α-Fe precipitates may be multidomain magnetic particles as the critical size for Fe goes from 15 nm for spherical particles to about 60 nm for ellipsoidal particles with an aspect ratio 10:1.[11] This FM–AFM coexistence has also been found in many other granular alloys.[12] Moreover, if the surface layer were the cause of the AFM correlations, we note that a two-dimensional Heisenberg system with AFM interactions does not show long-range order and the susceptibility displays a very broad maximum with temperature. Finally, a surface spin-disordered structure might also contribute to the outer loop. That disorder might arise from either a reduced number of Fe neighbors for surface spins (leading to a frustrated magnetic structure or to superparamagnetism), charge transfer or particle/matrix interdiffusion, among others.

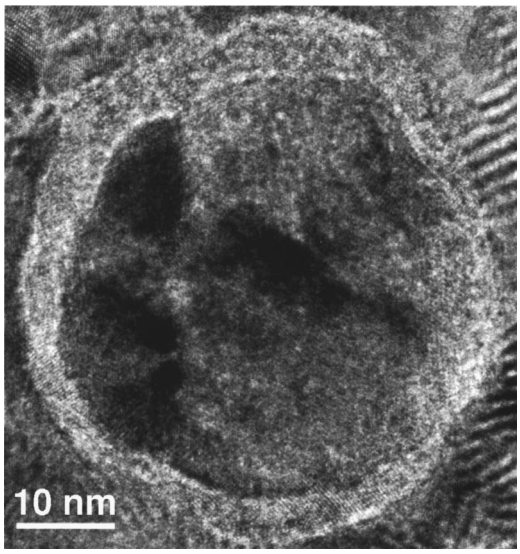

FIG. 9. HRTEM image for an α-Fe precipitate in sample D, suggesting the existence of a surface layer of a few nanometer in thickness with a structure different from the particle core.

Preliminary HRTEM images of the particle/matrix interface suggest that some particles had a surface layer of a few nanometers (Fig. 9) with neither the structure of the particle core nor the matrix. The lattice images from the surface layer, calibrated using the fringes from the $\text{Cu}_{[110]}$ matrix, might be attributed to γ-Fe. Also, the presence in the samples of an Fe–O-type compound was studied by XPS and EELS. XPS spectra were taken by using a Mg Kα source, after cleaning the surface by ion milling. The spectrum for sample D [Fig. 10(a)] shows the $2p_{1/2}$ and $2p_{3/2}$ lines for metallic Cu, the Auger lines for Cu and the 1s line ($\sim$284 eV) for C. The latter suggests some residual surface contamination after cleaning. Neither Cu–O nor O lines were ob-

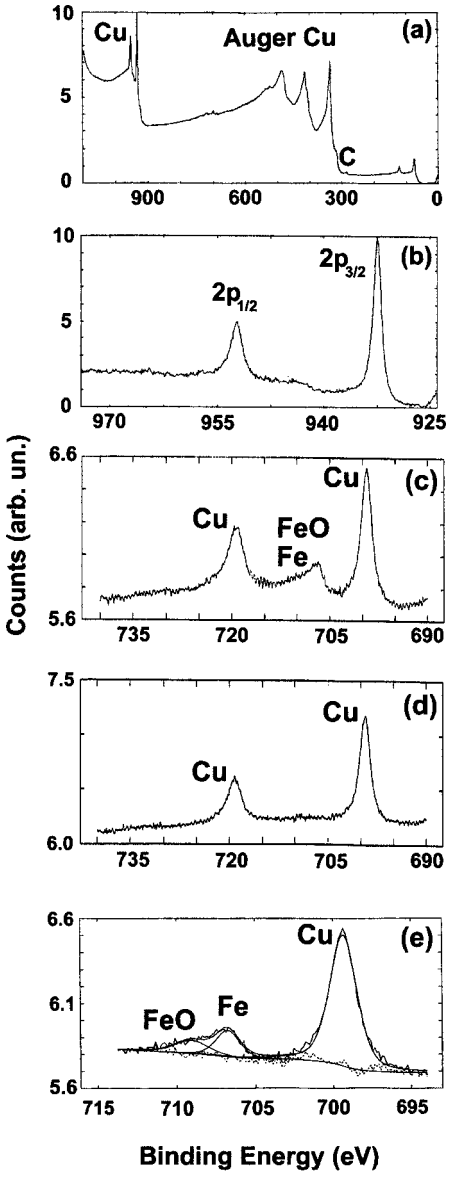

FIG. 10. XPS data for sample D after cleaning the sample surface by ion milling: (a) spectrum in the binding energy range 200–1000 eV, using a Mg $K\alpha$ source, (b) detail of (a) in the range 925–970 eV, showing the $2p_{1/2}$ and $2p_{3/2}$ contributions from metallic Cu, (c) detail of (a) in the range 695–740 eV, showing the contributions from metallic Cu (cross-talking effect due to the indirect excitation of the Al $K\alpha$ source which is placed near that of Mg $K\alpha$), metallic Fe and an Fe–O-type compound, (d) detail of the spectrum in the same binding energy range as (c) for a metallic Cu standard using a Mg $K\alpha$ source and showing the cross-talking effect with the Al $K\alpha$ source, and (e) best fitting of the $2p_{3/2}$ peaks in (c), leading to an average composition 98.1 at. % metallic Cu–1.2 at. % metallic Fe–0.7 at. % FeO.

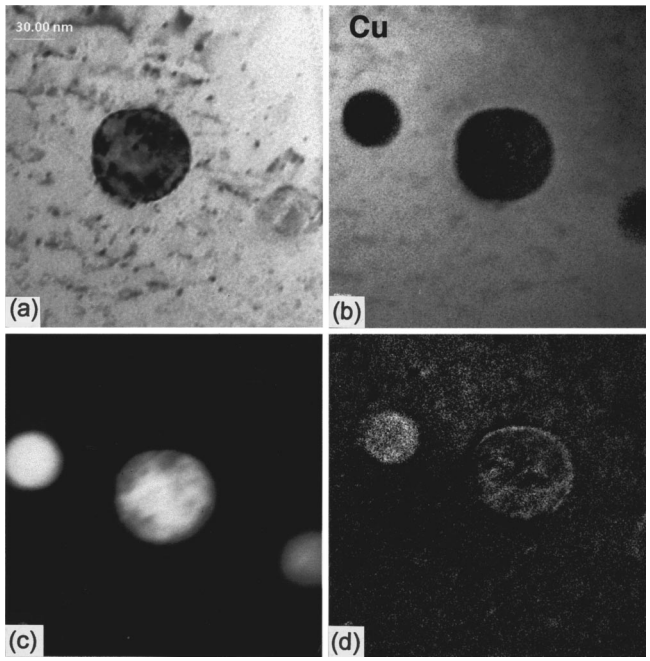

FIG. 11. Energy filtered maps obtained from EELS, for sample D: (a) HRTEM image, (b) Cu mapping, (c) Fe mapping, and (d) O mapping. All spectra were performed after cleaning the sample surface by ion milling in LN_2.

served. A detail of the spectrum in the binding energy range 925–970 eV clearly shows the $2p_{1/2}$ and $2p_{3/2}$ lines for metallic Cu, with binding energies of ~953 and ~933 eV, respectively [Fig. 10(b)]. A detail of the spectrum in the range 690–740 eV is shown in Fig. 10(c). The main lines in this spectrum, at ~699 eV and ~719 eV, do not correspond to Fe but to Cu, and this arises from a cross-talking effect between the Mg and Al $K\alpha$ sources; although we are using the Mg K α source, the Al one sits beside it, such that the excitation of the Mg anode leads to a residual excitation of that of Al. The spectrum for a pure metallic Cu standard [Fig. 10(d)] using the Mg $K\alpha$ source reinforces this experimental artifact—the spectrum for Cu appears not only at the expected energy of ~933 ($2p_{1/2}$) and ~953 eV ($2p_{3/2}$) (not shown), but also at ~699 and ~719 eV, respectively. The difference between these two sets of values (~234 eV) corresponds to the difference between the in-coming energies of the $K\alpha$ radiation of the Al and Mg sources. Fortunately, the Fe contribution to the spectrum in Fig. 10(c) is clearly shown within the range 705–715 eV. However, it is evident that the expected line at ~707 eV ($2p_{3/2}$) broadens to higher energies, suggesting that not only metallic Fe but a compound of iron and oxygen is present. The best fit of the spectrum is shown in Fig. 10(e), with the contribution of FeO ($2p_{3/2}$ at ~709 eV), leading to an average composition of 98.1 at. % metallic Cu, 1.2 at. % metallic Fe, and 0.7 at. % FeO, for sample D. Finally, the energy filtered maps for Cu, Fe, and O obtained by EELS (Fig. 11) reinforce the suggestion that there is an extra amount of O in the surface layer around the metallic α-Fe particles, probably associated with the FeO detected by XPS.

In summary, if we assume the ratio of metallic Fe to FeO obtained by XPS to be correct, 63% of the Fe content in the precipitates is metallic and 37% is oxide. However, according to the hysteresis measurements, only about 30% of the total Fe content contributes to the net magnetization (α-Fe). The expected solubility of Fe in Cu is about 0.35 at. % for sample D (which results in about 12% in the average composition $Cu_{97}Fe_3$), as the phase diagram and the ac susceptibility both suggest. We may thus estimate that the γ-Fe phase in sample D is about 21% of the Fe content, that is, 0.6 at. %. Consequently, this is why XRD, TEM, and the other

experimental techniques used in this study cannot clearly ascertain the γ-Fe precipitates, particularly, if these precipitates are coherent with the Cu matrix.

ACKNOWLEDGMENTS

X.B. wants to thank the Catalonian government for a grant to visit the Lawrence Berkeley Laboratory (LBL) from July 1997 to February 1998 and in January and November 1999, within the framework of the ''Gaspar de Portolà'' Catalonian Studies Program (Catalonia-California) and the ACI98-14 Joint Action. K.M.K. was also partially supported by this grant during his visit to the University of Barcelona (UB) in June 1998. It is a pleasure to acknowledge J. Bassas (UB) for XRD and Dr. P. Gorostiza (UB) and Dr. L. Calvo (UB) for the XPS measurements. X.B. is indebted to Dr. J. Turner (LBL) for image processing and Professor A. Labarta (UB) for many fruitful discussions. Financial support of the Spanish CICYT through the MAT97-0404 project is gratefully recognized. Work at LBNL was supported by the Director, Office of Energy Research, Office of Basic Energy Sciences, Materials Sciences Division of the U.S. Department of Energy under Contract No. DE-AC03-76SF00098.

[1] A. Berkowitz, J. R. Mitchell, M. J. Carey, A. P. Young, S. Zhang, F. E. Spada, F. T. Parker, H. Hutten, and G. Thomas, Phys. Rev. Lett. **68**, 3745 (1992).
[2] J. Q. Xiao, J. S. Jiang, and C. L. Chien, Phys. Rev. Lett. **68**, 3749 (1992).
[3] See, for example, *Magnetic Properties of Metals. d-Elements, Alloys and Compounds*, in Data in Science and Technology, edited by H. P. J. Wijn and R. Poerschke (Springer, Berlin, 1991).
[4] See, for example, F. Badia, X. Batlle, A. Labarta, M. L. Watson, A. B. Johnston, and J. N. Chapman, J. Appl. Phys. **82**, 677 (1997).
[5] See, for example, F. Badia, G. Fratucello, B. Martinez, D. Fiorani, A. Labarta, and J. Tejada, J. Magn. Magn. Mater. **93**, 425 (1991), and references therein.
[6] For extensive data see, Landolt-Boernstein, volume III/19, subvolumes a and b (unpublished).
[7] O. Kubaschewski *et al.*, Z. Metallkd. **68**, 495 (1977); G. Salje *et al.*, Z. Metallkd. **69**, 197 (1978).
[8] See, for example, T. Fujii, Y. Watanabe, T. Enami, A. Sato, and M. Sato, The Iron and Steel Institute of Japan (ISIJ) International **32**, 1027 (1992); T. Fujii, T. Mori, and M. Kato, Acta Metall. Mater. **40**, 3413 (1992).
[9] J. L. Dormann, D. Fiorani, and E. Tronc, Adv. Chem. Phys. **XCVIII**, 283 (1997).
[10] J. I. Guittleman, B. Abeles, and S. Bonzowski, Phys. Rev. B **9**, 3891 (1974).
[11] *The Physical Principles of Magnetism*, edited by A. H. Morrish (Wiley, New York, 1965).
[12] See for example, X. Batlle, V. Franco, A. Labarta, M. L. Watson, and K. O'Grady, Appl. Phys. Lett. **70**, 132 (1997).